

# Excitation spectra, spin structures, and entanglement characteristics of four-electron double-quantum-dot artificial molecules

Ying Li, Constantine Yannouleas,\* and Uzi Landman†

*School of Physics, Georgia Institute of Technology, Atlanta, Georgia 30332-0430*

(Dated: 30 January 2009)

Energy spectra, spin configurations, and entanglement characteristics of a system of four electrons in lateral double quantum dots are investigated using exact diagonalization (EXD), as a function of interdot separation, applied magnetic field, and strength of interelectron repulsion. A distinctly different quantum behavior is found compared to that of circular single quantum dots. As a function of the magnetic field, the energy spectra exhibit a low-energy band consisting of a group of six states, with the number six being a consequence of the conservation of the total spin of the four electrons and the ensuing spin degeneracies. These six states appear to cross at a single value of the magnetic field, with the crossing point becoming sharper for larger interdot distances. As the strength of the Coulomb repulsion increases, the six states tend to become degenerate and a well defined energy gap separates them from the higher-in-energy excited states.

The appearance of the low-energy band is a consequence of the formation of a Wigner supermolecule, with the four electrons (two in each dot) being localized at the vertices of a rectangular parallelogram. Using the spin-resolved pair-correlation functions, one can map the EXD many-body wave functions onto the spin functions associated with the four localized electrons. Analogies with nanomagnets, such as finite Heisenberg clusters, are discussed. The ability to determine associated spin functions enables investigations concerning entanglement properties of the system of four electrons. In particular, the formation of Wigner supermolecules generates EXD solutions belonging to the class of strongly entangled states referred to as  $N$ -qubit Dicke states in the quantum-information literature.

PACS numbers: 73.21.La, 31.15.V-, 03.67.Mn, 03.65.Ud

## I. INTRODUCTION

The field of two-dimensional (2D) semiconductor quantum dots (QDs) has witnessed rapid expansion in the last several years, both experimentally<sup>1,2</sup> and theoretically.<sup>3,4,5</sup> Along with fundamental interest in the properties of such systems, and as a test ground for highly correlated electrons, a major motivation for these growing endeavors has been the promising outlook and potential of quantum dots concerning the implementation of solid-state quantum computing and quantum information devices.<sup>6,7,8</sup> To this effect highly precise control of the space and spin degrees of freedom of a small number  $N$  of confined electrons (down to an empty<sup>9,10,11</sup> QD) needs to be achieved, and experimentally this was demonstrated recently for two electrons in a lateral double quantum dot molecule (see Ref. 2, and references therein). From the theoretical standpoint, high-level computational methods that reach beyond the level of mean-field approximation are needed,<sup>5</sup> with the ability to provide solutions that preserve all the symmetries of the many-body Hamiltonian. For example, conservation of total spin is essential for describing spin entanglement in small assemblies of electrons that exhibit localization in space. Such assemblies may be viewed as finite Heisenberg spin clusters<sup>12,13</sup> whose quantum behavior (due to finite-size fluctuations and correlation effects) differs drastically from the behavior expected from magnetic systems in the thermodynamic limit.<sup>12,14</sup>

There is an abundance of experimental and theoretical publications concerning *circular single* quantum dots

with a small number of electrons.<sup>1,3,4,5,15,16,17</sup> In this paper, we use exact diagonalization<sup>5</sup> (EXD) to investigate the properties of *lateral double quantum dots* (DQDs) containing four electrons. DQDs are referred to also as artificial molecules. DQDs containing two electrons have been already studied extensively both experimentally<sup>2</sup> and theoretically.<sup>5,18,19</sup> However, experimental studies of DQDs with three or four electrons have not been performed as yet; we are aware of a single theoretical study of a lateral DQD with three electrons,<sup>20</sup> and another one of two laterally coupled quantum rings with three electrons.<sup>21</sup>

In light of the novel quantum behavior discovered in our investigations (compared to circular QDs, both concerning the spectra and entanglement aspects), we hope that the present work would serve as an impetus for further experimental studies on lateral DQDs. In particular, as a function of the magnetic field, we find that: (1) A low-energy band of six states develops as the strength of the Coulomb repulsion increases, separated by an energy gap from the other excited states, and (2) All six states appear to “cross” at a single value of the magnetic field. The crossing point gets sharper for larger interdot distances. We find that the specific number of crossing states (six) derives from the spin degeneracies and multiplicities expressed by the branching diagram.<sup>22</sup>

The formation of the low-energy band is a consequence of the localization of the four electrons within each dot (with two electrons in each dot). This localization leads to formation (with increasing strength of the Coulomb repulsion) of a Wigner supermolecule,<sup>23</sup> with the four lo-

calized electrons (two in each dot) being located at the corners of a rectangular parallelogram. Using the spin-resolved pair-correlation functions, we show how to map the EXD many-body wave functions onto the spin functions associated with the four localized electrons. This mapping leads us naturally to study analogies with finite systems described by a model Heisenberg Hamiltonian (often referred to as finite Heisenberg clusters). We further discuss that the determination of the equivalent spin functions enables investigations concerning the entanglement properties of the EXD solutions. In particular, we show that the formation of Wigner supermolecules leads to strongly entangled states known in the literature of quantum information as  $N$ -qubit Dicke states.<sup>24,25,26,27</sup>

We finally mention that the trends in the excitation spectra (e.g., formation of a low-energy band) and entanglement properties (e.g., mapping to spin functions of localized electrons) found in the case of a double quantum dots have many analogies with those found in other deformed configurations, and in particular single anisotropic quantum dots; see, e.g., the case of three electrons in Ref. 28.

## II. TWO-DIMENSIONAL TWO-CENTER-OSCILLATOR CONFINING POTENTIAL

In the two-dimensional two-center-oscillator (TCO), the single-particle levels associated with the confining potential of the artificial molecule are determined by the single-particle hamiltonian<sup>29</sup>

$$H = T + \frac{1}{2}m^*\omega_y^2y^2 + \frac{1}{2}m^*\omega_{xk}^2x_k'^2 + V_{neck}(x) + h_k + \frac{g^*\mu_B}{\hbar}\mathbf{B} \cdot \mathbf{s}, \quad (1)$$

where  $x_k' = x - x_k$  with  $k = 1$  for  $x < 0$  (left) and  $k = 2$  for  $x > 0$  (right), and the  $h_k$ 's control the relative well-depth, thus allowing studies of hetero-QDMs.  $y$  denotes the coordinate perpendicular to the interdot axis ( $x$ ).  $T = (\mathbf{p} - e\mathbf{A}/c)^2/2m^*$ , with  $\mathbf{A} = 0.5(-By, Bx, 0)$ , and the last term in Eq. (1) is the Zeeman interaction with  $g^*$  being the effective  $g$  factor,  $\mu_B$  the Bohr magneton, and  $\mathbf{s}$  the spin of an individual electron. The most general shapes described by  $H$  are two semiellipses connected by a smooth neck [ $V_{neck}(x)$ ].  $x_1 < 0$  and  $x_2 > 0$  are the centers of these semiellipses,  $d = x_2 - x_1$  is the interdot distance, and  $m^*$  is the effective electron mass.

For the smooth neck, we use  $V_{neck}(x) = \frac{1}{2}m^*\omega_{xk}^2[\mathcal{C}_kx_k'^3 + \mathcal{D}_kx_k'^4]\theta(|x| - |x_k|)$ , where  $\theta(u) = 0$  for  $u > 0$  and  $\theta(u) = 1$  for  $u < 0$ . The four constants  $\mathcal{C}_k$  and  $\mathcal{D}_k$  can be expressed via two parameters, as follows:  $\mathcal{C}_k = (2 - 4\epsilon_k^b)/x_k$  and  $\mathcal{D}_k = (1 - 3\epsilon_k^b)/x_k^2$ , where the barrier-control parameters  $\epsilon_k^b = (V_b - h_k)/V_{0k}$  are related to the actual (controlable) height of the bare interdot barrier ( $V_b$ ) between the two QDs, and  $V_{0k} = m^*\omega_{xk}^2x_k^2/2$  (for  $h_1 = h_2$ ,  $V_{01} = V_{02} = V_0$ ).

The single-particle levels of  $H$ , including an external perpendicular magnetic field  $B$ , are obtained by numerical diagonalization in a (variable-with-separation) basis consisting of the eigenstates of the auxiliary (zero-field) hamiltonian:

$$H_0 = \frac{\mathbf{p}^2}{2m^*} + \frac{1}{2}m^*\omega_y^2y^2 + \frac{1}{2}m^*\omega_{xk}^2x_k'^2 + h_k. \quad (2)$$

The eigenvalue problem associated with the auxiliary hamiltonian [Eq. (2)] is separable in  $x$  and  $y$ , i.e., the wave functions are written as

$$\varphi_i(x, y) = X_\mu(x)Y_n(y), \quad (3)$$

with  $i \equiv \{\mu, n\}$ ,  $i = 1, 2, \dots, K$ .

The  $Y_n(y)$  are the eigenfunctions of a one-dimensional oscillator, and the  $X_\mu(x \leq 0)$  or  $X_\mu(x > 0)$  can be expressed through the parabolic cylinder functions<sup>30,31</sup>  $U[\gamma_k, (-1)^k \xi_k]$ , where  $\xi_k = x_k' \sqrt{2m^*\omega_{xk}/\hbar}$ ,  $\gamma_k = (-E_x + h_k)/(\hbar\omega_{xk})$ , and  $E_x = (\mu + 0.5)\hbar\omega_{x1} + h_1$  denotes the  $x$ -eigenvalues. The matching conditions at  $x = 0$  for the left and right domains yield the  $x$ -eigenvalues and the eigenfunctions  $X_\mu(x)$ . The  $n$  indices are integer. The number of  $\mu$  indices is finite; however, they are in general real numbers.

In the Appendix, we discuss briefly the energy spectra associated with the single-particle states of the two-center oscillator Hamiltonian given by Eq. (1). We follow there the notation presented first in Ref. 32. For further details, see Ref. 33.

In this paper, we will limit ourselves to QDMs with  $x_2 = -x_1$  and  $\hbar\omega_y = \hbar\omega_{x1} = \hbar\omega_{x2} = \hbar\omega_0$ . However, in several instances we will compare with the case of a single elliptic QD where  $x_2 = -x_1 = 0$  and  $\hbar\omega_y \neq \hbar\omega_x = \hbar\omega_{x1} = \hbar\omega_{x2}$ . In all cases, we will use  $\hbar\omega_0 = 5.1$  meV,  $m^* = 0.070m_e$  (this effective-mass value corresponds to GaAs), and  $K = 50$  (which guarantees numerical convergence<sup>34</sup>).

## III. THE MANY-BODY HAMILTONIAN AND THE EXACT DIAGONALIZATION METHOD

The many-body hamiltonian  $\mathcal{H}$  for a dimeric QDM comprising  $N$  electrons can be expressed as a sum of the single-particle part  $H(i)$  defined in Eq. (1) and the two-particle interelectron Coulomb repulsion,

$$\mathcal{H} = \sum_{i=1}^N H(i) + \sum_{i=1}^N \sum_{j>i}^N \frac{e^2}{\kappa r_{ij}}, \quad (4)$$

where  $\kappa$  is the dielectric constant and  $r_{ij}$  denotes the relative distance between the  $i$  and  $j$  electrons.

As we mentioned in the introduction, we will use the method of exact diagonalization for determining<sup>33</sup> the solution of the many-body problem specified by the hamiltonian (4).

In the EXD method, one writes the many-body wave function  $\Phi_N^{\text{EXD}}(\mathbf{r}_1, \mathbf{r}_2, \dots, \mathbf{r}_N)$  as a linear superposition

of Slater determinants  $\Psi^N(\mathbf{r}_1, \mathbf{r}_2, \dots, \mathbf{r}_N)$  that span the many-body Hilbert space and are constructed out of the single-particle *spin-orbitals*

$$\chi_j(x, y) = \varphi_j(x, y)\alpha, \quad \text{if } 1 \leq j \leq K, \quad (5)$$

and

$$\chi_j(x, y) = \varphi_{j-K}(x, y)\beta, \quad \text{if } K < j \leq 2K, \quad (6)$$

where  $\alpha(\beta)$  denote up (down) spins. Namely

$$\Phi_{N,q}^{\text{EXD}}(\mathbf{r}_1, \dots, \mathbf{r}_N) = \sum_I C_I^q \Psi_I^N(\mathbf{r}_1, \dots, \mathbf{r}_N), \quad (7)$$

where

$$\Psi_I^N = \frac{1}{\sqrt{N!}} \begin{vmatrix} \chi_{j_1}(\mathbf{r}_1) & \dots & \chi_{j_N}(\mathbf{r}_1) \\ \vdots & \ddots & \vdots \\ \chi_{j_1}(\mathbf{r}_N) & \dots & \chi_{j_N}(\mathbf{r}_N) \end{vmatrix}, \quad (8)$$

and the master index  $I$  counts the number of arrangements  $\{j_1, j_2, \dots, j_N\}$  under the restriction that  $1 \leq j_1 < j_2 < \dots < j_N \leq 2K$ . Of course,  $q = 1, 2, \dots$  counts the excitation spectrum, with  $q = 1$  corresponding to the ground state.

The exact diagonalization of the many-body Schrödinger equation

$$\mathcal{H}\Phi_{N,q}^{\text{EXD}} = E_{N,q}^{\text{EXD}}\Phi_{N,q}^{\text{EXD}} \quad (9)$$

transforms into a matrix diagonalization problem, which yields the coefficients  $C_I^q$  and the EXD eigenenergies  $E_{N,q}^{\text{EXD}}$ . Because the resulting matrix is sparse, we implement its numerical diagonalization employing the well known ARPACK solver.<sup>35</sup>

The matrix elements  $\langle \Psi_N^I | \mathcal{H} | \Psi_N^J \rangle$  between the basis determinants [see Eq. (8)] are calculated using the Slater rules.<sup>36</sup> Naturally, an important ingredient in this respect are the two-body matrix elements of the Coulomb interaction,

$$\frac{e^2}{\kappa} \int_{-\infty}^{\infty} \int_{-\infty}^{\infty} d\mathbf{r}_1 d\mathbf{r}_2 \varphi_i^*(\mathbf{r}_1) \varphi_j^*(\mathbf{r}_2) \frac{1}{|\mathbf{r}_1 - \mathbf{r}_2|} \varphi_k(\mathbf{r}_1) \varphi_l(\mathbf{r}_2), \quad (10)$$

in the basis formed out of the single-particle spatial orbitals  $\varphi_i(\mathbf{r})$ ,  $i = 1, 2, \dots, K$ . In our approach, these matrix elements are determined numerically.

The Slater determinants  $\Psi_I^N$  [see Eq. (8)] conserve the third projection  $S_z$ , but not the square  $\hat{\mathbf{S}}^2$  of the total spin. However, because  $\hat{\mathbf{S}}^2$  commutes with the many-body hamiltonian, the EXD solutions are automatically eigenstates of  $\hat{\mathbf{S}}^2$  with eigenvalues  $S(S+1)$ . After the diagonalization, these eigenvalues are determined by applying  $\hat{\mathbf{S}}^2$  onto  $\Phi_{N,q}^{\text{EXD}}$  and using the relation

$$\hat{\mathbf{S}}^2 \Psi_I^N = \left[ (N_\alpha - N_\beta)^2 / 4 + N/2 + \sum_{i < j} \varpi_{ij} \right] \Psi_I^N, \quad (11)$$

where the operator  $\varpi_{ij}$  interchanges the spins of electrons  $i$  and  $j$  provided that their spins are different;  $N_\alpha$  and  $N_\beta$  denote the number of spin-up and spin-down electrons, respectively.

Of great help in reducing the size of the matrices to be diagonalized is the fact that the parity (with respect to the origin) of the EXD many-body wave function is a good quantum number for all values of the magnetic field when  $h_1 = h_2$ . Specifically, the  $xy$ -parity operator associated with reflections about the origin of the axes is defined as

$$\hat{\mathcal{P}}_{xy} \Phi_{N,q}^{\text{EXD}}(\mathbf{r}_1, \mathbf{r}_2, \mathbf{r}_3, \mathbf{r}_4) = \Phi_{N,q}^{\text{EXD}}(-\mathbf{r}_1, -\mathbf{r}_2, -\mathbf{r}_3, -\mathbf{r}_4) \quad (12)$$

and has eigenvalues  $\pm 1$ .

One can also consider partial parity operators  $\hat{\mathcal{P}}_x$  and  $\hat{\mathcal{P}}_y$  associated solely with reflections about the  $x$  and  $y$  axis, respectively; of course  $\hat{\mathcal{P}}_{xy} = \hat{\mathcal{P}}_x \hat{\mathcal{P}}_y$ . We note that unlike  $\hat{\mathcal{P}}_{xy}$ , the partial parities  $\hat{\mathcal{P}}_x$  and  $\hat{\mathcal{P}}_y$  are conserved only for zero magnetic fields ( $B = 0$ ). With the two-center oscillator *cartesian* basis that we use [see Eq. (3)], it is easy to calculate the parity eigenvalues for the Slater determinants, Eq. (8), that span the many-body Hilbert space. Because  $X_\mu(x)$  and  $Y_n(y)$  conserve the partial  $\hat{\mathcal{P}}_x$  and  $\hat{\mathcal{P}}_y$  parities, respectively, one finds:

$$\hat{\mathcal{P}}_{xy} \Psi_I^N = (-)^{\sum_{i=1}^4 m_i + n_i} \Psi_I^N, \quad (13)$$

where  $m_i$  and  $n_i$  count the number of single-particle states associated with the bare two-center oscillator [see the auxiliary hamiltonian  $H_0$  in Eq. (2)] along the  $x$  axis and the simple oscillator along the  $y$  direction (with the assumption that the lowest states have  $m = 0$  and  $n = 0$ , since they are even states). We note again that the index  $\mu$  in Eq. (3) is not an integer in general, while  $m$  here is indeed an integer (since it counts the number of single-particle states along the  $x$  direction).

#### IV. MANY-BODY SPIN EIGENFUNCTIONS

For completeness and for the reader's convenience, we outline in this section several well established (but often not well known) properties of the many-body spin eigenfunctions which are useful for analyzing the trends and behavior of the spin multiplicities exhibited by the EXD wave functions for  $N = 4$  electrons. We stress here that the ability to describe spin multiplicities is an advantage of the EXD method compared to the more familiar spin-density functional approaches whose single-determinantal wave functions preserve only the third projection  $S_z$  of the total spin, and thus are subject to "spin contamination" errors. As we will discuss below, the spin multiplicities of the EXD wave functions lead naturally to formation of highly entangled Dicke states.<sup>24,25,26,27</sup>

A basic property of spin eigenfunctions is that they exhibit degeneracies for  $N > 2$ , i.e., there may be more than one linearly independent (and orthogonal) spin functions

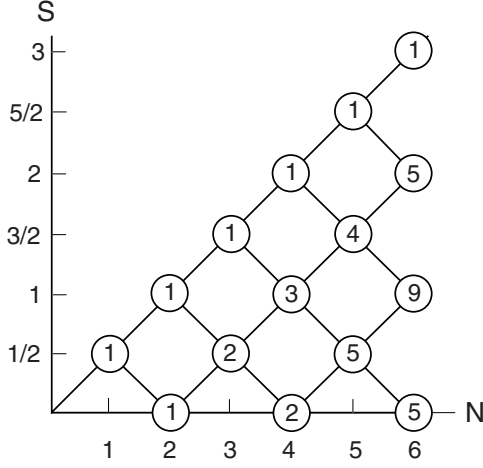


FIG. 1: The branching diagram for the spin degeneracies. The total-spin quantum number  $S$  is given on the vertical axis, and the number of particles,  $N$ , on the horizontal one. The numbers inside the circles give the number,  $g(N, S)$ , of linear independent (and orthogonal) spin functions for the corresponding values of  $N$  and  $S$ .

that are simultaneous eigenstates of both  $\hat{\mathbf{S}}^2$  and  $S_z$ . These degeneracies are usually visualized by means of the *branching diagram*<sup>22</sup> displayed in Fig. 1. The axes in this plot describe the number  $N$  of fermions (horizontal axis) and the quantum number  $S$  of the total spin (vertical axis). At each point  $(N, S)$ , a circle is drawn containing the number  $g(N, S)$  which gives the degeneracy of spin states. It is found<sup>22</sup> that

$$g(N, S) = \binom{N}{N/2 - S} - \binom{N}{N/2 - S - 1}. \quad (14)$$

Specifically for  $N = 4$  particles, there is one spin eigenfunction with  $S = 2$ , three with  $S = 1$ , and two with  $S = 0$ . In general the spin part of the EXD wave functions involves a linear superposition over all the degenerate spin eigenfunctions for a given  $S$ .

In the case of zero magnetic field and for a small number of particles, one can find compact expressions that encompass all possible superpositions. For example, for  $N = 4$  and  $S = 0$ ,  $S_z = 0$  one has:<sup>37</sup>

$$\begin{aligned} \mathcal{X}_{00} = & \sqrt{\frac{1}{3}} \sin \theta |\uparrow\uparrow\downarrow\downarrow\rangle + \left(\frac{1}{2} \cos \theta - \sqrt{\frac{1}{12}} \sin \theta\right) |\uparrow\downarrow\uparrow\downarrow\rangle \\ & - \left(\frac{1}{2} \cos \theta + \sqrt{\frac{1}{12}} \sin \theta\right) |\uparrow\downarrow\downarrow\uparrow\rangle \\ & - \left(\frac{1}{2} \cos \theta + \sqrt{\frac{1}{12}} \sin \theta\right) |\downarrow\uparrow\uparrow\downarrow\rangle \\ & + \left(\frac{1}{2} \cos \theta - \sqrt{\frac{1}{12}} \sin \theta\right) |\downarrow\uparrow\downarrow\uparrow\rangle + \sqrt{\frac{1}{3}} \sin \theta |\downarrow\downarrow\uparrow\uparrow\rangle, \end{aligned} \quad (15)$$

where the parameter  $\theta$  satisfies  $-\pi/2 \leq \theta \leq \pi/2$  and is chosen such that  $\theta = 0$  corresponds to the spin function

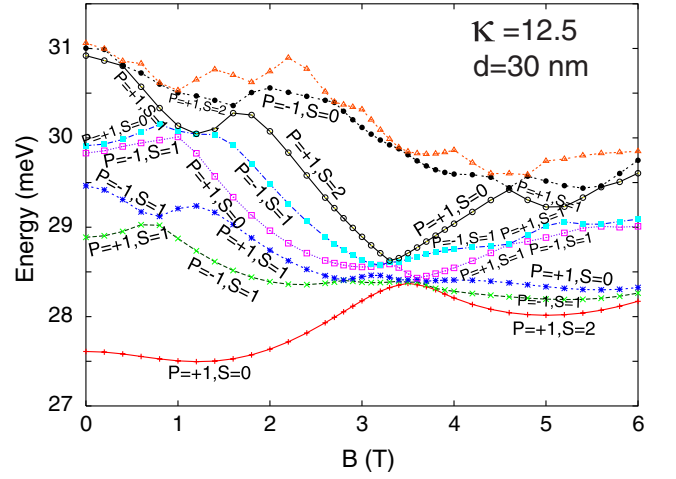


FIG. 2: Energy spectra (as a function of the magnetic field  $B$ ) for  $N = 4$  electrons in a double quantum dot with interdot separation  $d = 30$  nm. Case of weak interelectron repulsion corresponding to GaAs ( $\kappa = 12.5$ ). The calculation were done for the case  $S_z = 0$  and the Zeeman term was neglected. In this case all states with the same total spin  $S$  and different spin projections  $S_z$  are degenerate. The effect of the Zeeman term can be easily added. Remaining parameters:  $\epsilon^b = 0.5$ ,  $\hbar\omega_0 = 5.1$  meV,  $m^* = 0.07m_e$ . For all figures, the parameters  $\hbar\omega_0$  and  $m^*$  are kept the same (see Section II). Energies are referenced to  $N\hbar\sqrt{\omega_0^2 + \omega_c^2/4}$ , where  $\omega_c = eB/(m^*c)$  is the cyclotron frequency.

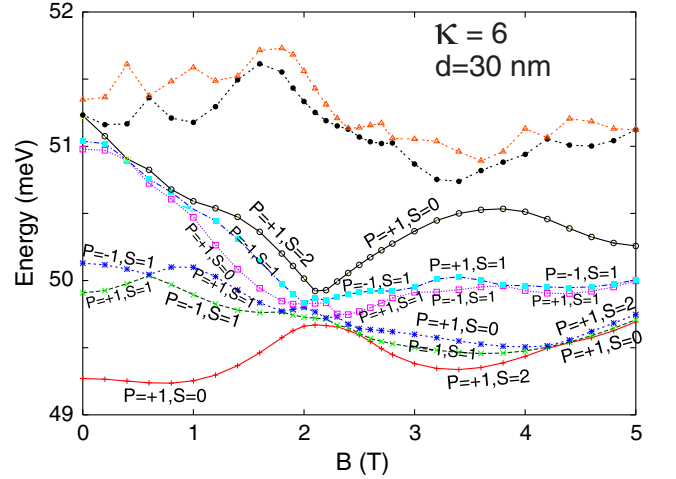


FIG. 3: Energy spectra (as a function of the magnetic field  $B$ ) for  $N = 4$  electrons in a double quantum dot with interdot separation  $d = 30$  nm. Case of intermediate interelectron repulsion ( $\kappa = 6$ ). The interdot barrier corresponds to  $\epsilon^b = 0.5$ . Energies are referenced to  $N\hbar\sqrt{\omega_0^2 + \omega_c^2/4}$ , where  $\omega_c = eB/(m^*c)$  is the cyclotron frequency.

with intermediate two-electron spin  $S_{12} = 0$  and three-electron spin  $S_{123} = 1/2$ ; whereas  $\theta = \pm\pi/2$  corresponds to the one with intermediate spins  $S_{12} = 1$  and  $S_{123} = 1/2$ .

For  $N = 4$  and  $S = 1$ ,  $S_z = 0$  one has:

$$\begin{aligned}
\mathcal{X}_{10} = & \\
& \left( \sqrt{\frac{1}{6}} \sin \theta \sin \varphi - \sqrt{\frac{1}{12}} \sin \theta \cos \varphi - \frac{1}{2} \cos \theta \right) |\downarrow\uparrow\uparrow\downarrow\rangle \\
& + \left( \sqrt{\frac{1}{6}} \sin \theta \sin \varphi - \sqrt{\frac{1}{12}} \sin \theta \cos \varphi + \frac{1}{2} \cos \theta \right) |\uparrow\downarrow\uparrow\downarrow\rangle \\
& + \left( \sqrt{\frac{1}{12}} \sin \theta \cos \varphi - \sqrt{\frac{1}{6}} \sin \theta \sin \varphi - \frac{1}{2} \cos \theta \right) |\downarrow\uparrow\downarrow\uparrow\rangle \\
& + \left( \sqrt{\frac{1}{12}} \sin \theta \cos \varphi - \sqrt{\frac{1}{6}} \sin \theta \sin \varphi + \frac{1}{2} \cos \theta \right) |\uparrow\downarrow\downarrow\uparrow\rangle \\
& + \left( \sqrt{\frac{1}{6}} \sin \theta \sin \varphi + \sqrt{\frac{1}{3}} \sin \theta \cos \varphi \right) |\uparrow\uparrow\downarrow\downarrow\rangle \\
& - \left( \sqrt{\frac{1}{6}} \sin \theta \sin \varphi + \sqrt{\frac{1}{3}} \sin \theta \cos \varphi \right) |\downarrow\downarrow\uparrow\uparrow\rangle, \quad (16)
\end{aligned}$$

where the parameters  $\theta$  and  $\varphi$  satisfy  $-\pi/2 \leq \theta \leq \pi/2$  and  $-\pi/2 \leq \varphi \leq \pi/2$ . Three independent spin functions with definite intermediate two-electron,  $S_{12}$ , and three-electron,  $S_{123}$ , spin values correspond to the  $\theta$  and  $\varphi$  values as follows: for  $S_{12} = 0$  and  $S_{123} = 1/2$ ,  $\theta = 0$ ; for  $S_{12} = 1$  and  $S_{123} = 1/2$ ,  $\theta = \pm\pi/2$  and  $\varphi = 0$ ; and for  $S_{12} = 1$  and  $S_{123} = 3/2$ ,  $\theta = \pm\pi/2$  and  $\varphi = \pm\pi/2$ .

Finally, for  $N = 4$  and  $S = 2$ ,  $S_z = 0$  (maximum polarization) case, one has:

$$\mathcal{X}_{20} = \frac{|\downarrow\downarrow\uparrow\uparrow\rangle + |\downarrow\uparrow\downarrow\uparrow\rangle + |\downarrow\uparrow\uparrow\downarrow\rangle + |\uparrow\downarrow\downarrow\uparrow\rangle + |\uparrow\downarrow\uparrow\downarrow\rangle + |\uparrow\uparrow\downarrow\downarrow\rangle}{\sqrt{6}}. \quad (17)$$

## V. RESULTS: ENERGY SPECTRA

The excitation spectra as a function of the applied magnetic field for four electrons in a double QD with interdot distance  $d = 2x_2 = -2x_1 = 30$  nm and no voltage bias between the dots [ $h_1 = h_2 = 0$ , see Eq. (1)] are plotted for three different values of the interelectron repulsion strength, i.e., weak [ $\kappa = 12.5$  (GaAs); see Fig. 2], intermediate ( $\kappa = 6$ ; see Fig. 3), and strong ( $\kappa = 2$ ; see Fig. 4) Coulomb repulsion. The interdot barrier parameter was taken as  $\epsilon^b = 0.5$  (because  $h_1 = h_2 = 0$ , one has  $\epsilon_1^b = \epsilon_2^b = \epsilon^b$ ; see Section II for the definitions). In all cases, we calculated the eight lowest energy levels.

We observe that the lowest six levels form a band that separates from the rest of the spectrum through the opening of a gap. This happens already at a relatively weak interelectron repulsion, and it is well developed for the intermediate case ( $\kappa = 6$ ). It is of interest to note that the number of levels in the band (six) coincides with the total number of spin eigenfunctions for  $N = 4$  fermions, as can be seen from the branching diagram displaying the spin degeneracies. In particular, there is one level with total spin  $S = 2$  (and parity  $\mathcal{P}_{xy} = 1$ ), three levels with total spin  $S = 1$  (two with  $\mathcal{P}_{xy} = 1$  and one with

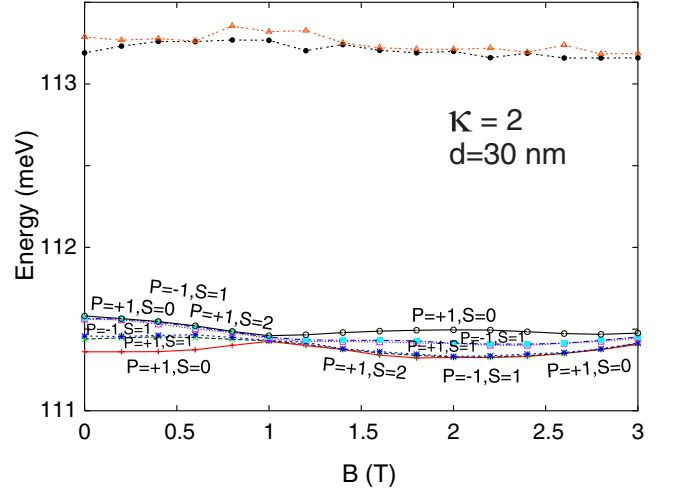


FIG. 4: Energy spectra (as a function of the magnetic field  $B$ ) for  $N = 4$  electrons in a double quantum dot with interdot separation  $d = 30$  nm. Case of strong interelectron repulsion ( $\kappa = 2$ ). The interdot barrier corresponds to  $\epsilon^b = 0.5$ . Energies are referenced to  $N\hbar\sqrt{\omega_0^2 + \omega_c^2/4}$ , where  $\omega_c = eB/(m^*c)$  is the cyclotron frequency.

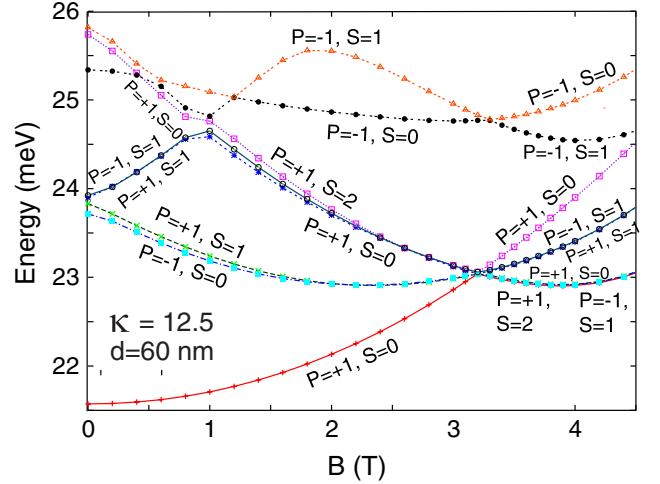


FIG. 5: Energy spectra (as a function of the magnetic field  $B$ ) for  $N = 4$  electrons in a double quantum dot with interdot separation  $d = 60$  nm. Case of weak interelectron repulsion corresponding to GaAs ( $\kappa = 12.5$ ). The interdot barrier corresponds to  $\epsilon^b = 0.5$ . Energies are referenced to  $N\hbar\sqrt{\omega_0^2 + \omega_c^2/4}$ , where  $\omega_c = eB/(m^*c)$  is the cyclotron frequency.

$\mathcal{P}_{xy} = -1$ ), and two levels with total spin  $S = 0$  (one with  $\mathcal{P}_{xy} = 1$  and the second with  $\mathcal{P}_{xy} = -1$ ). All these six levels approximately cross at one point situated at about  $B \approx 3.5$  T for  $\kappa = 12.5$  and  $B \approx 2.2$  T for  $\kappa = 6$ .

The trends associated with the opening of a gap and the formation of a six-state low band appear further reinforced for the larger interdot distance of  $d = 60$  nm (displayed in Figs. 5 – 7 for the three values of the dielectric

constant  $\kappa = 12.5, 6,$  and  $2,$  respectively). It is remarkable that the six lower curves cross now at a sharply defined point (situated at  $B \approx 3.3$  T for  $\kappa = 12.5$  and  $B \approx 2.1$  T for  $\kappa = 6$ ). The six curves demonstrate additional near degeneracies regrouping approximately to three curves before and after the crossing point, which results in a remarkable simplification of the spectrum.

For strong repulsion ( $\kappa = 2$ ), all six states in the low band are practically degenerate for both distances ( $d = 30$  nm ; see Fig. 4 and  $d = 60$  nm; see Fig. 7). This is a consequence of the formation of a near-rigid Wigner molecule (WM) with strongly localized electrons. Namely, the overlap between the orbitals of localized electrons are practically zero (see, e.g., Ref. 23), yielding a vanishing exchange,<sup>38</sup> and thus all six possible spin multiplicities become degenerate in energy. Furthermore the physical picture of a near-rigid Wigner molecule suggests that the energy gap to the next band of states corresponds to excitation of the lowest stretching vibrational mode of the 4-electron molecule.

It is natural to anticipate at this point that the above behavior at low  $B$  can be generalized to an arbitrary number of electrons  $N$  in a double QD. Namely, as the strength of the interelectron interaction increases, a low-energy band comprising all possible spin multiplicities will form and it will become progressively well separated by an energy gap from the higher excitations. For example, for  $N = 6$ , an inspection of the branching diagram in Fig. 1 leads us to the prediction that there will be 20 states in this low-energy band. A similar behavior emerges also in the case of a *single*, but strongly *anisotropic* quantum dot; indeed a low-energy band of three states (see the branching diagram in Fig. 1) has been found for  $N = 3$  electrons in Ref. 28.

It is of interest to contrast the above behavior of the excitation spectra in a double QD with that of an  $N$ -electron circular dot. Specifically, in the circular QD, large interelectron repulsion leads to formation of a near-rigid *rotating* Wigner molecule that exhibits a rigid moment of inertia. Then the states inside the low-energy band (two states for  $N = 2$ , three for  $N = 3$ , six for  $N = 4$ , etc.) do not become degenerate in energy, but form an yrast rotational band<sup>39</sup> specified by  $L^2/2\mathcal{J}_0$ , where  $L$  is the total angular momentum and  $\mathcal{J}_0$  is the classical moment of inertia. We note that the energy splittings among the yrast rotational states are much smaller than the vibrational energy gap in circular dots associated with the quantum of energy  $\sqrt{3}\hbar\omega_0$  of the stretching (often referred to as breathing) mode of the polygonal-ring configuration of the quasiclassical Wigner molecule.<sup>40,41,42</sup>

## VI. RESULTS: ELECTRON DENSITIES

The electron density is the expectation value of the one-body operator

$$\hat{\rho}(\mathbf{r}) = \sum_{i=1}^N \delta(\mathbf{r} - \mathbf{r}_i), \quad (18)$$

that is:

$$\begin{aligned} \rho(\mathbf{r}) &= \langle \Phi_{N,q}^{\text{EXD}} | \hat{\rho}(\mathbf{r}) | \Phi_{N,q}^{\text{EXD}} \rangle \\ &= \sum_{I,J} C_I^{q*} C_J^q \langle \Psi_I^N | \hat{\rho}(\mathbf{r}) | \Psi_J^N \rangle. \end{aligned} \quad (19)$$

Since  $\hat{\rho}(\mathbf{r})$  is a one-body operator, it connects only Slater determinants  $\Psi_I^N$  and  $\Psi_J^N$  that differ at most by *one* spin orbital  $\chi_j(\mathbf{r})$ ; for the corresponding Slater rules for calculating matrix elements between determinants for one-body operators in terms of spin orbitals, see Table 2.3 in Ref. 36.

In Figs. 8(a-f), we display (for the aforementioned three strengths of interelectron repulsion) the ground-state electron densities for for  $N = 4$  electrons in the case of a double dot at zero magnetic field with interdot separations  $d = 30$  nm (left column) and  $d = 60$  nm (right column).

For the weak interaction case ( $\kappa = 12.5$ ) at  $B = 0$ , the electron densities do not exhibit clear signatures of formation of a Wigner molecule for either interdot distance,  $d = 30$  nm [Fig. 8(a)] or  $d = 60$  nm [Fig. 8(b)]. The Wigner molecule is well formed, however, in the case of the intermediate Coulomb repulsion [ $\kappa = 6$ ; see Figs. 8(c-d)]. One observes indeed four humps that correspond to

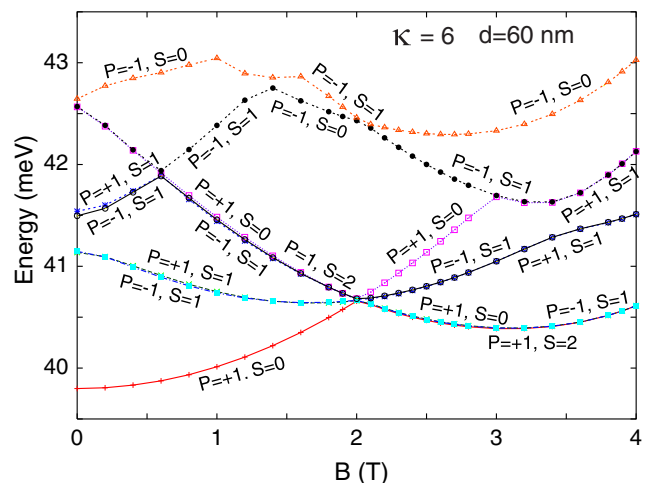


FIG. 6: Energy spectra (as a function of the magnetic field  $B$ ) for  $N = 4$  electrons in a double quantum dot with interdot separation  $d = 60$  nm. Case of intermediate interelectron repulsion ( $\kappa = 6$ ). The interdot barrier corresponds to  $\epsilon^b = 0.5$ . Energies are referenced to  $N\hbar\sqrt{\omega_0^2 + \omega_c^2/4}$ , where  $\omega_c = eB/(m^*c)$  is the cyclotron frequency.

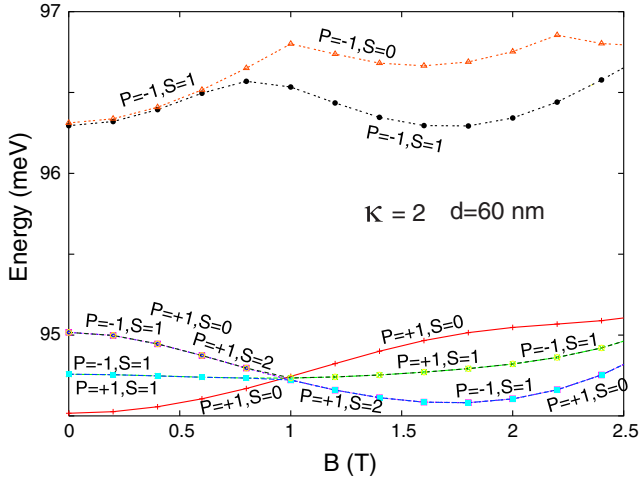


FIG. 7: Energy spectra (as a function of the magnetic field  $B$ ) for  $N = 4$  electrons in a double quantum dot with interdot separation  $d = 60$  nm. Case of strong repulsion ( $\kappa = 2$ ). The interdot barrier corresponds to  $\epsilon^b = 0.5$ . Energies are referenced to  $N\hbar\sqrt{\omega_0^2 + \omega_c^2}/4$ , where  $\omega_c = eB/(m^*c)$  is the cyclotron frequency.

the four localized electrons; they are located at  $(\pm 34.88$  nm,  $\pm 13.13$  nm) in the  $d = 60$  nm case. In the case of strong Coulomb repulsion ( $\kappa = 2$ ) and for the same interdot distance  $d = 60$  nm, the electrons are further localized as can be seen from Fig. 8(f); the four humps occur now at  $(\pm 39.86$  nm,  $\pm 21.02$  nm). The Wigner molecule is also well formed in the the strong-repulsion and  $d = 30$  nm case, as can be seen from Fig. 8(e), with the localized electrons located at  $(\pm 29.28$  nm,  $\pm 21.11$  nm).

## VII. RESULTS: SPIN-RESOLVED CONDITIONAL PROBABILITY DISTRIBUTIONS AT $B = 0$

### A. Definitions

In the regime corresponding to a well-defined Wigner molecule, the electron densities (see Sect. VI) are characterized by four humps that reflect the localization of the four electrons in the double quantum dot. Such charge densities do not provide any information concerning the spin structure of each EXD state. In fact, all six EXD states in the lower band exhibit very similar four-humped electron densities.

The spin configurations associated with a given  $(S, S_z)$  EXD state in the WM regime can be explored with the help of the spin-resolved two-point anisotropic correlation function defined as:

$$P_{\sigma\sigma_0}(\mathbf{r}, \mathbf{r}_0) = \langle \Phi_{N,q}^{\text{EXD}} | \sum_{i \neq j} \delta(\mathbf{r} - \mathbf{r}_i) \delta(\mathbf{r}_0 - \mathbf{r}_j) \delta_{\sigma\sigma_i} \delta_{\sigma_0\sigma_j} | \Phi_{N,q}^{\text{EXD}} \rangle, \quad (20)$$

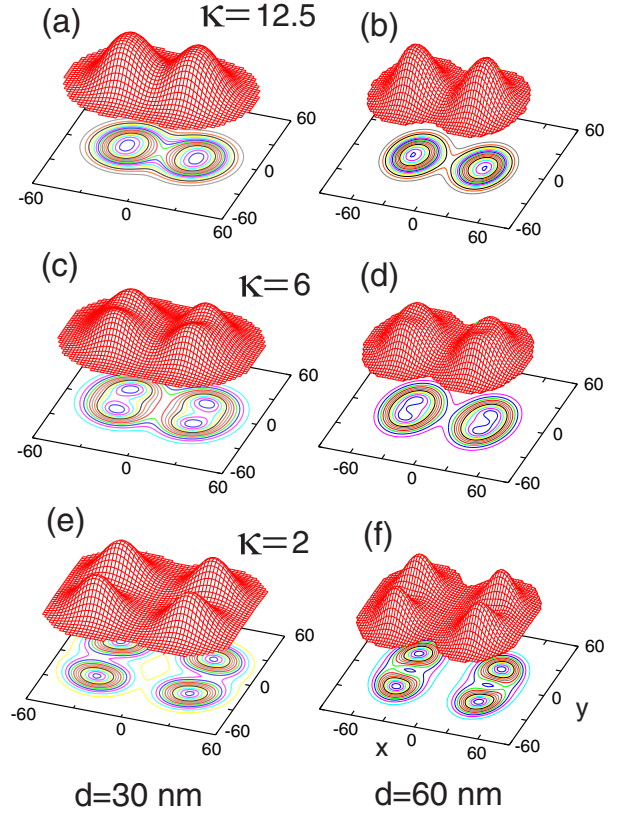


FIG. 8: Electron density at  $B = 0$  for the ground state (with  $S = 0$ ,  $S_z = 0$ , parity  $P_{xy} = 1$ ) for  $N = 4$  electrons in a double quantum dot with interdot separations  $d = 30$  nm (left column) and  $d = 60$  nm (right column). The top (a-b), middle (c-d), and bottom (e-f) rows correspond to  $\kappa = 12.5$  (weak repulsion),  $\kappa = 6$  (intermediate repulsion), and  $\kappa = 2$  (strong repulsion), respectively. Ground-state energies: (a)  $E = 27.609$  meV, (b)  $E = 21.572$  meV, (c)  $E = 49.217$  meV, (d)  $E = 39.799$  meV, (e)  $E = 111.361$  meV, (f)  $E = 94.516$  meV (compare Figs. 2–7). The interdot barrier corresponds to  $\epsilon^b = 0.5$ . Distances in nm. Vertical axis in arbitrary units (with the same scale for all six panels).

with the EXD many-body wave function given by equation (7).

Using a normalization constant

$$\mathcal{N}(\sigma, \sigma_0, \mathbf{r}_0) = \int P_{\sigma\sigma_0}(\mathbf{r}, \mathbf{r}_0) d\mathbf{r}, \quad (21)$$

we further define a related conditional probability distribution (CPD) as

$$\mathcal{P}_{\sigma\sigma_0}(\mathbf{r}, \mathbf{r}_0) = P_{\sigma\sigma_0}(\mathbf{r}, \mathbf{r}_0) / \mathcal{N}(\sigma, \sigma_0, \mathbf{r}_0), \quad (22)$$

having the property  $\int \mathcal{P}_{\sigma\sigma_0}(\mathbf{r}, \mathbf{r}_0) d\mathbf{r} = 1$ . The spin-resolved CPD gives the spatial probability distribution of finding a second electron with spin projection  $\sigma$  under the condition that another electron is located (fixed) at  $\mathbf{r}_0$  with spin projection  $\sigma_0$ ;  $\sigma$  and  $\sigma_0$  can be either up ( $\uparrow$ ) or down ( $\downarrow$ ).

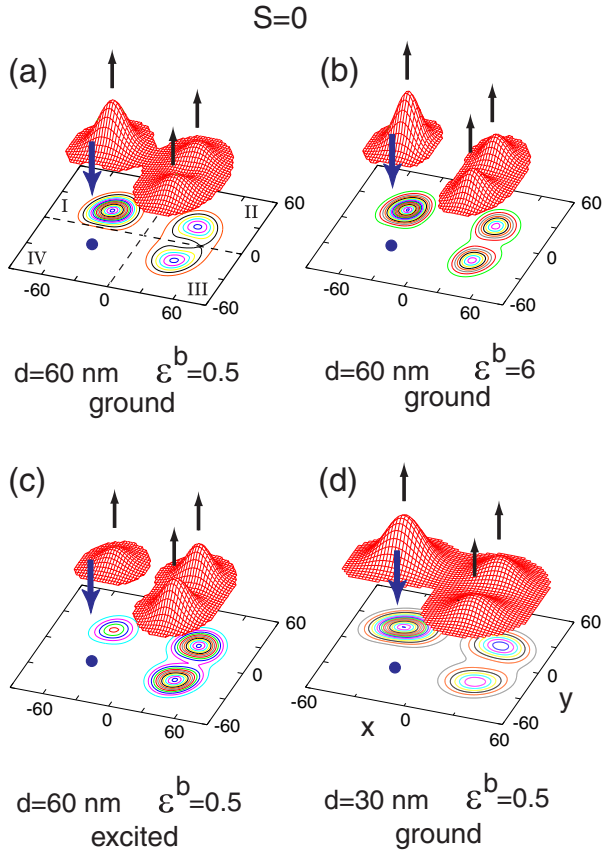


FIG. 9: CPDs  $\mathcal{P}_{\uparrow\downarrow}$  at  $B = 0$  for several EXD states with  $S = 0, S_z = 0$ , and parity  $P_{xy} = 1$  of  $N = 4$  electrons in a double quantum dot with interdot separations  $d = 60$  nm (a-c) and  $d = 30$  nm (d). Case of strong Coulomb repulsion ( $\kappa = 2$ ) with an interdot barrier  $\epsilon^b = 0.5$  (a,c-d) and  $\epsilon^b = 6$  (b). Panels (a-b,d) correspond to ground states. Panel (c) corresponds to the excited second  $S = 0$  state for the same parameters as in panel (a) (see Fig. 7 and the branching diagram in Fig. 1). Energies: (a)  $E = 94.516$  meV, (b)  $E = 96.811$  meV, (c)  $E = 95.017$  meV, and (d)  $E = 111.361$  meV (compare Figs. 4 and 7). Distances in nm. Vertical axis in arbitrary units (with the same scale for all panels in Figs. 9 – 11). The fixed point is located at the maximum of the hump in the lower-left quadrant of the corresponding electron density, i.e., at  $\mathbf{r}_0 = (-40$  nm,  $-21$  nm) for panels (a-c) and  $\mathbf{r}_0 = (-29$  nm,  $-19$  nm) for panel (d).

To calculate  $P_{\sigma\sigma_0}(\mathbf{r}, \mathbf{r}_0)$  in Eq. (20), we use a symmetrized operator

$$\hat{T}_{\sigma\sigma_0}(\mathbf{r}, \mathbf{r}_0) = \sum_{i < j} [\delta(\mathbf{r} - \mathbf{r}_i) \delta(\mathbf{r}_0 - \mathbf{r}_j) \delta_{\sigma\sigma_i} \delta_{\sigma_0\sigma_j} + \delta(\mathbf{r} - \mathbf{r}_j) \delta(\mathbf{r}_0 - \mathbf{r}_i) \delta_{\sigma\sigma_j} \delta_{\sigma_0\sigma_i}], \quad (23)$$

yielding

$$\begin{aligned} P_{\sigma\sigma_0}(\mathbf{r}, \mathbf{r}_0) &= \langle \Phi_{N,q}^{\text{EXD}} | \hat{T} | \Phi_{N,q}^{\text{EXD}} \rangle \\ &= \sum_{I,J} C_I^{q*} C_J^q \langle \Psi_I^N | \hat{T} | \Psi_J^N \rangle. \end{aligned} \quad (24)$$

Since  $\hat{T}_{\sigma\sigma_0}(\mathbf{r}, \mathbf{r}_0)$  is a two-body operator, it connects only Slater determinants  $\Psi_I^N$  and  $\Psi_J^N$  that differ at most by *two* spin orbitals  $\chi_{j_1}(\mathbf{r})$  and  $\chi_{j_2}(\mathbf{r})$ ; for the corresponding Slater rules for calculating matrix elements between determinants for two-body operators in terms of spin orbitals, see Table 2.4 in Ref. 36.

## B. Examples of $S = 0, S_z = 0$ EXD states

For each charge density corresponding to a given state of the system, one can plot four different spin-resolved CPDs, i.e.,  $\mathcal{P}_{\uparrow\uparrow}$ ,  $\mathcal{P}_{\uparrow\downarrow}$ ,  $\mathcal{P}_{\downarrow\uparrow}$ , and  $\mathcal{P}_{\downarrow\downarrow}$ . This can potentially lead to a very large number of time consuming computations and an excessive number of plots. For studying the spin structure of the  $S = 0, S_z = 0$  states at  $B = 0$ , however, we found that knowledge of a single CPD, taken here to be  $\mathcal{P}_{\uparrow\downarrow}$  (see Fig. 9), is sufficient in the regime of Wigner-molecule formation. Indeed, the specific angle  $\theta$  specifying the spin function  $\mathcal{X}_{00}$  Eq. (15) corresponding to the CPDs portrayed in Fig. 9 can be determined through the procedure described in the following:

We designate with roman indices *I*, *II*, *III*, and *IV* the four quadrants of the  $(x, y)$  plane, starting with the upper left quadrant and going clockwise [see Fig. 9(a)]. In the case of a  $4e$  Wigner-molecule, a single electron is localized within each quadrant. The same roman indices designate also the positions of the localized electrons in each of the six Slater determinants (e.g.,  $|\uparrow\uparrow\downarrow\downarrow\rangle$ ,  $|\uparrow\downarrow\uparrow\downarrow\rangle$ , etc.) that enter into the spin function  $\mathcal{X}_{00}$  in Eq. (15). We take always the fixed point to correspond to the fourth (*IV*) quadrant [bottom left in Fig. 9(a)]. An inspection of Eq. (15) shows that only three Slater determinants in  $\mathcal{X}_{00}$  contribute to  $\mathcal{P}_{\uparrow\downarrow}$ , namely  $|\uparrow\uparrow\downarrow\downarrow\rangle$ ,  $|\uparrow\downarrow\uparrow\downarrow\rangle$ , and  $|\downarrow\uparrow\uparrow\downarrow\rangle$ ; these are the only determinants in Eq. (15) with a down spin in the 4th quadrant. From these three Slater determinants, only the first and the second contribute to the conditional probability  $\Pi_{\uparrow\downarrow}(I)$  of finding another electron with spin-up in quadrant *I*; this corresponds to the volume under the hump of the EXD CPD in quadrant *I* [see, e.g., the hump in Fig. 9(a)]. Taking the squares of the coefficients of  $|\uparrow\uparrow\downarrow\downarrow\rangle$  and  $|\uparrow\downarrow\uparrow\downarrow\rangle$  in Eq. (15), one gets

$$\Pi_{\uparrow\downarrow}(I) \propto \frac{\sin^2 \theta}{3} + \left( \frac{1}{2} \cos \theta - \sqrt{\frac{1}{12}} \sin \theta \right)^2. \quad (25)$$

Similarly, one finds that only  $|\uparrow\uparrow\downarrow\downarrow\rangle$  and  $|\downarrow\uparrow\uparrow\downarrow\rangle$  contribute to  $\Pi_{\uparrow\downarrow}(II)$ , and that

$$\Pi_{\uparrow\downarrow}(II) \propto \frac{\sin^2 \theta}{3} + \left( \frac{1}{2} \cos \theta + \sqrt{\frac{1}{12}} \sin \theta \right)^2. \quad (26)$$

Integrating under the humps of the EXD CPD in quadrants *I* and *II*, we determine numerically the ratio  $\Pi_{\uparrow\downarrow}(I)/\Pi_{\uparrow\downarrow}(II)$ , which allows us to specify the absolute value of  $\theta$  (within the interval  $-90^\circ \leq \theta \leq 90^\circ$ ) via the

expressions in Eqs. (25) and (26). The restriction to the absolute value of  $\theta$  is a result of the squares of the sine and cosine entering in  $\Pi_{\uparrow\downarrow}(I)$  and  $\Pi_{\uparrow\downarrow}(III)$ . To obtain the actual sign of  $\theta$ , additional information is needed: for example the ratio  $\Pi_{\uparrow\downarrow}(I)/\Pi_{\uparrow\downarrow}(III)$  can be used in a similar way, where

$$\Pi_{\uparrow\downarrow}(III) \propto \left( \frac{1}{2} \cos \theta - \sqrt{\frac{1}{12}} \sin \theta \right)^2 + \left( \frac{1}{2} \cos \theta + \sqrt{\frac{1}{12}} \sin \theta \right)^2. \quad (27)$$

Using the method described above, we find that  $\theta \approx -60^\circ$  for the EXD ground state at  $d = 60$  nm (larger interdot distance) and  $\kappa = 2$  [strong repulsion; see Fig. 9(a)], and the corresponding spin function simplifies to

$$\mathcal{X}_{00}^{(1)} = -\frac{1}{2} |\uparrow\uparrow\downarrow\downarrow\rangle + \frac{1}{2} |\uparrow\downarrow\uparrow\downarrow\rangle + \frac{1}{2} |\downarrow\uparrow\downarrow\uparrow\rangle - \frac{1}{2} |\downarrow\downarrow\uparrow\uparrow\rangle. \quad (28)$$

Remarkably, increasing the interdot barrier from  $\epsilon^b = 0.5$  [Fig. 9(a)] to  $\epsilon^b = 6$  [Fig. 9(b)], while keeping the other parameters constant, does not influence much the composition of the associated spin function, which remains that given by Eq. (28). This happens in spite of the visible change in the degree of localization in the electronic orbitals, with the higher interdot-barrier case exhibiting a sharper localization.

In Fig. 9(c), we display the  $\mathcal{P}_{\uparrow\downarrow}$  CPD for an excited state with  $S = 0, S_z = 0$  (having  $P_{xy} = 1$  and energy  $E = 95.017$  meV), with the remaining parameters being the same as in Fig. 9(a). For this case, following an analysis as described above, we found the angle  $\theta \approx 30^\circ$ , which is associated with a spin function of the form

$$\begin{aligned} \mathcal{X}_{00}^{(2)} = & \frac{1}{2\sqrt{3}} |\uparrow\uparrow\downarrow\downarrow\rangle + \frac{1}{2\sqrt{3}} |\uparrow\downarrow\uparrow\downarrow\rangle - \frac{1}{\sqrt{3}} |\uparrow\downarrow\uparrow\uparrow\rangle \\ & - \frac{1}{\sqrt{3}} |\downarrow\uparrow\downarrow\downarrow\rangle + \frac{1}{2\sqrt{3}} |\downarrow\uparrow\downarrow\uparrow\rangle + \frac{1}{2\sqrt{3}} |\downarrow\downarrow\uparrow\uparrow\rangle. \end{aligned} \quad (29)$$

We note that the spin functions in Eqs. (28) and (29) are orthogonal.

In Fig. 9(d), we display the  $\mathcal{P}_{\uparrow\downarrow}$  CPD for the ground state with  $S = 0, S_z = 0$  (having  $P_{xy} = 1$  and energy  $E = 111.361$  meV) and for the shorter interdot distance  $d = 30$  nm. For this case, we found an angle  $\theta \approx -63.08^\circ$ , which corresponds to the following spin function:

$$\begin{aligned} \mathcal{X}_{00}^{(3)} = & -0.5148 |\uparrow\uparrow\downarrow\downarrow\rangle + 0.4838 |\uparrow\downarrow\uparrow\downarrow\rangle + 0.031 |\uparrow\downarrow\uparrow\uparrow\rangle \\ & 0.031 |\downarrow\uparrow\downarrow\downarrow\rangle + 0.4838 |\downarrow\uparrow\downarrow\uparrow\rangle - 0.5148 |\downarrow\downarrow\uparrow\uparrow\rangle. \end{aligned} \quad (30)$$

From a comparison of the above result with that for the larger  $d = 60$  nm [see Eq. (28)], we conclude that the difference in interdot distance results in a slight variation of the spin functions.

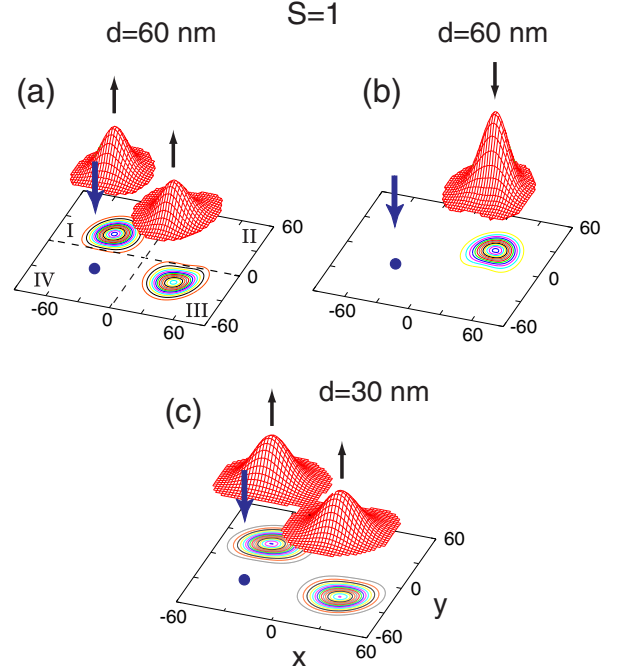


FIG. 10: CPDs at  $B = 0$  for excited EXD states with  $S = 1, S_z = 0$ , and parity  $P_{xy} = 1$  of  $N = 4$  electrons in a double quantum dot at the larger interdot separation  $d = 60$  nm (a-b) and the shorter interdot separation  $d = 30$  nm (c). Panels (a) and (c) display  $\mathcal{P}_{\uparrow\downarrow}$  CPDS (down-up), while panel (b) displays a different  $\mathcal{P}_{\downarrow\downarrow}$  CPD (down-down), but for the *same* state as in (a). Case of strong Coulomb repulsion ( $\kappa = 2$ ) with interdot barrier  $\epsilon^b = 0.5$ . Energies: (a-b)  $E = 94.757$  meV, and (c)  $E = 111.438$  meV (compare Figs. 4 and 7). Distances in nm. Vertical axis in arbitrary units (with the same scale for all panels in Figs. 9 – 11). The fixed point is located at the maximum of the hump in the lower-left quadrant of the corresponding electron density, i.e., at  $\mathbf{r}_0 = (-40$  nm,  $-21$  nm) for panels (a-b) and  $\mathbf{r}_0 = (-29$  nm,  $-19$  nm) for panel (c). Note that this is a case with  $S = 1$ ; the previous Fig. 9 displayed  $S = 0$  cases.

### C. Examples of $S = 1, S_z = 0$ EXD states

In this section, we turn our attention to partially polarized EXD states with  $S = 1$ .

In Fig. 10(a), we display the  $\mathcal{P}_{\uparrow\downarrow}$  CPD at  $B = 0$  for an excited state with  $S = 1, S_z = 0$ , parity  $P_{xy} = 1$ , and energy  $E = 94.757$  meV, at the larger interdot separation  $d = 60$  nm. Again we consider the case of strong Coulomb repulsion ( $\kappa = 2$ ) with an interdot barrier  $\epsilon^b = 0.5$ . The corresponding spin function  $\mathcal{X}_{10}$  [Eq. (16)] depends on two different angles  $\theta$  and  $\phi$ , and one needs at least two different CPDs for determining their specific values. For this purpose, we display also the  $\mathcal{P}_{\downarrow\downarrow}$  CPD for the same state in Fig. 10(b).

The specific values of  $\theta$  and  $\phi$  associated with the CPDs in Figs. 10(a) and 10(b) can be determined through the ratios  $\Pi_{\uparrow\downarrow}(I)/\Pi_{\uparrow\downarrow}(II)$  and  $\Pi_{\uparrow\downarrow}(I)/\Pi_{\uparrow\downarrow}(III)$  [associated with Fig. 10(a)] and  $\Pi_{\downarrow\downarrow}(I)/\Pi_{\downarrow\downarrow}(II)$  and

$\Pi_{\downarrow\downarrow}(I)/\Pi_{\downarrow\downarrow}(III)$  [associated with Fig. 10(b)], where

$$\begin{aligned} \Pi_{\uparrow\downarrow}(I) &\propto \frac{1}{3} \sin^2 \theta \sin^2 \phi + \frac{5}{12} \sin^2 \theta \cos^2 \phi + \frac{1}{4} \cos^2 \theta \\ &+ \frac{\sqrt{2}}{6} \sin^2 \theta \sin \phi \cos \phi + \frac{1}{\sqrt{6}} \sin \theta \cos \theta \sin \phi \\ &- \frac{1}{\sqrt{12}} \sin \theta \cos \theta \cos \phi, \end{aligned} \quad (31)$$

$$\begin{aligned} \Pi_{\uparrow\downarrow}(II) &\propto \frac{1}{3} \sin^2 \theta \sin^2 \phi + \frac{5}{12} \sin^2 \theta \cos^2 \phi + \frac{1}{4} \cos^2 \theta \\ &+ \frac{\sqrt{2}}{6} \sin^2 \theta \sin \phi \cos \phi - \frac{1}{\sqrt{6}} \sin \theta \cos \theta \sin \phi \\ &+ \frac{1}{\sqrt{12}} \sin \theta \cos \theta \cos \phi, \end{aligned} \quad (32)$$

$$\begin{aligned} \Pi_{\uparrow\downarrow}(III) &\propto \frac{1}{3} \sin^2 \theta \sin^2 \phi + \frac{1}{6} \sin^2 \theta \cos^2 \phi \\ &- \frac{\sqrt{2}}{3} \sin^2 \theta \sin \phi \cos \phi + \frac{1}{2} \cos^2 \theta, \end{aligned} \quad (33)$$

and

$$\Pi_{\downarrow\downarrow}(I) \propto \left( \sqrt{\frac{1}{6}} \sin \theta \sin \phi - \sqrt{\frac{1}{12}} \sin \theta \cos \phi - \frac{1}{2} \cos \theta \right)^2, \quad (34)$$

$$\Pi_{\downarrow\downarrow}(II) \propto \left( \sqrt{\frac{1}{6}} \sin \theta \sin \phi - \sqrt{\frac{1}{12}} \sin \theta \cos \phi + \frac{1}{2} \cos \theta \right)^2, \quad (35)$$

$$\Pi_{\downarrow\downarrow}(III) \propto \left( \sqrt{\frac{1}{6}} \sin \theta \sin \phi + \sqrt{\frac{1}{3}} \sin \theta \cos \phi \right)^2. \quad (36)$$

Using Eqs. (31) – (36) and the numerical values of the ratios  $\Pi_{\uparrow\downarrow}(I)/\Pi_{\uparrow\downarrow}(II)$  and  $\Pi_{\uparrow\downarrow}(I)/\Pi_{\uparrow\downarrow}(III)$ ,  $\Pi_{\downarrow\downarrow}(I)/\Pi_{\downarrow\downarrow}(II)$  and  $\Pi_{\downarrow\downarrow}(I)/\Pi_{\downarrow\downarrow}(III)$  (specified via a volume integration under the humps of the EXD CPDs), we determined that  $\theta = -45^\circ$  and  $\sin \phi = -\sqrt{2/3}$ ,  $\cos \phi = \sqrt{1/3}$  (i.e.,  $\phi \approx -54.736^\circ$ ). Thus, the corresponding spin function reduces to the simple form

$$\mathcal{X}_{10} = \sqrt{\frac{1}{2}} |\uparrow\downarrow\uparrow\downarrow\rangle - \sqrt{\frac{1}{2}} |\downarrow\uparrow\downarrow\uparrow\rangle. \quad (37)$$

In Fig. 10(c), we display the  $\mathcal{P}_{\uparrow\downarrow}$  CPD at  $B = 0$  for a similar excited state as in Fig. 10(a) (with  $S = 1$ ,  $S_z = 0$ , parity  $P_{xy} = 1$ , and energy  $E = 111.438$  meV) of  $N = 4$  electrons at the shorter interdot separation  $d = 30$  nm. Here too we consider the case of strong Coulomb repulsion ( $\kappa = 2$ ) with interdot barrier  $\epsilon^b = 0.5$ . We note that the localization of electrons is stronger for the larger interdot distance [compare Fig. 10(a) with Fig. 10(c)]. This difference, however, does not influence the coefficients entering into the associated spin function, which we found to remain very close to the specific form in Eq. (37).

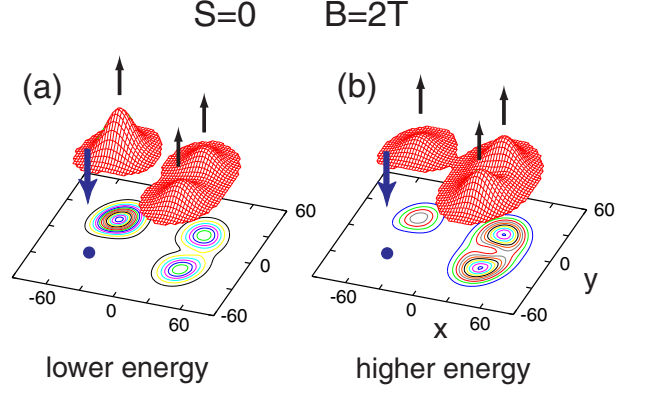


FIG. 11:  $\mathcal{P}_{\uparrow\downarrow}$  CPDs for the EXD states at  $B = 2$  T with  $S = 0$ ,  $S_z = 0$ , and parity  $P_{xy} = 1$  of  $N = 4$  electrons in a double quantum dot at the larger interdot separation  $d = 60$  nm. (a) The lower energy of the two  $S = 0$  states (see branching diagram in Fig. 1). (b) Higher energy  $S = 0$  state. Case of strong Coulomb repulsion ( $\kappa = 2$ ) with interdot barrier  $\epsilon^b = 0.5$ . Energies: (a)  $E = 94.605$  meV and (b)  $E = 95.047$  meV (compare Fig. 7). Distances in nm. Vertical axis in arbitrary units (with the same scale for all panels in Figs. 9 – 11). The fixed point is located at  $\mathbf{r}_0 = (-40 \text{ nm}, -21 \text{ nm})$ .

## VIII. RESULTS: SPIN-RESOLVED CONDITIONAL PROBABILITY DISTRIBUTIONS AT $B \neq 0$

In Fig. 11 we display EXD CPDs at a finite value of the magnetic field, and precisely at  $B = 2$  T, for the two states of the low-energy band with  $S = 0$ ,  $S_z = 0$  (at the larger interdot separation  $d = 60$  nm and strong interelectron repulsion  $\kappa = 2$ ). This value of  $B$  was chosen to lie beyond the crossing point for the six states of the low-energy band (which happens at  $B \sim 1$  T; see Fig. 7). Comparison with the CPDs of the corresponding states at zero magnetic field [see Figs. 9(a) and 9(c)] shows that the spin structure of the associated Wigner molecule varies rather slowly with the increasing magnetic field in the range  $0 \leq B \leq 2.5$  T.

Following the height of the humps in the left upper quadrants, one observes that the CPD in Fig. 11(a) (case of *lower-energy* state at  $B = 2$  T with  $S = 0$  and  $P_{xy} = 1$ ) corresponds to that of Fig. 9(a) (case of *lower-energy* state at  $B = 0$  with  $S = 0$  and  $P_{xy} = 1$ ). Similarly, the CPD in Fig. 11(b) at  $B = 2$  T (*higher-energy* state) corresponds to that of Fig. 9(c) at  $B = 0$  (*higher-energy* state). From these results, we conclude that the two states with  $S = 0$  and  $P_{xy} = 1$  do not really cross at the 'crossing' point at  $B \sim 1$  T. In reality, this point is an anticrossing point for these two states, although the anticrossing gap is too small to be seen with the naked eye. This behavior agrees with that expected from states having the same quantum numbers. We checked that a similar observation applies for the two other states in the low-energy band having the same quantum numbers, i.e., those having  $S = 1$  and  $P_{xy} = -1$ .

## IX. DISCUSSION

### A. Finite Heisenberg spin clusters

In VII, using the spin-resolved CPDs, we showed that the EXD many-body wave functions in the Wigner-molecule regime can be expressed as a linear superposition of a small number of Slater determinants and that this superposition exhibits the structure expected from the theory of many-body spin functions. This finding naturally suggests a strong analogy with the field of nanomagnets and quantum magnetism, usually studied via the explicitly spin-dependent model effective Hamiltonian known as the Heisenberg Hamiltonian,<sup>12,13,43</sup> given by:

$$\mathcal{H}'_H = \sum_{i,j} J_{ij} \mathbf{S}_i \cdot \mathbf{S}_j - \mathbf{Q} \sum_i \mathbf{S}_i, \quad (38)$$

where  $J_{ij}$  are the exchange integrals between spins on sites  $i$  and  $j$ . Even in its more familiar, simplest form

$$\mathcal{H}_H = J \sum_{\langle i,j \rangle} \mathbf{S}_i \cdot \mathbf{S}_j, \quad (39)$$

that is that of the spin-1/2 Heisenberg antiferromagnet with nearest-neighbor interactions only, it is well known that the zero-temperature (at  $B = 0$ ) solutions of Hamiltonian (39) involve radically different forms as a function of the geometry, dimensionality, and size.

It is natural to compare the EXD spin functions determined in Section VII with well known solutions of the Heisenberg Hamiltonian [Eq. (39)] when the four spins are located on four sites arranged in a perfect square.<sup>13,14</sup> (The perfect-square arrangement arises<sup>44</sup> also in the case of formation of a four-electron Wigner molecule in a single circular quantum dot.) In this case, the ground state of  $\mathcal{H}_H$  is the celebrated resonating valence bond (RVB) state<sup>13,14</sup> which forms the basic block in many theoretical approaches aiming at describing high-temperature superconductors.<sup>45</sup> The RVB state has quantum numbers  $S = 0$ ,  $S_z = 0$  and is given by<sup>13,14</sup>

$$\begin{aligned} \mathcal{X}_{00}^{\text{RVB}} = & \frac{1}{2\sqrt{3}} |\uparrow\uparrow\downarrow\downarrow\rangle + \frac{1}{2\sqrt{3}} |\uparrow\downarrow\downarrow\uparrow\rangle + \frac{1}{2\sqrt{3}} |\downarrow\downarrow\uparrow\uparrow\rangle \\ & + \frac{1}{2\sqrt{3}} |\downarrow\uparrow\uparrow\downarrow\rangle - \frac{1}{\sqrt{3}} |\uparrow\downarrow\uparrow\downarrow\rangle - \frac{1}{\sqrt{3}} |\downarrow\uparrow\downarrow\uparrow\rangle. \end{aligned} \quad (40)$$

Although the excited-state EXD  $\mathcal{X}_{00}^{(2)}$  in the quantum-double-dot case portrayed in Fig. 9(c) appears to be similar to the RVB  $\mathcal{X}_{00}^{\text{RVB}}$  [Eq. (40)], they are not equal. Indeed the coefficients of the pair of Slater determinants  $|\uparrow\downarrow\uparrow\downarrow\rangle$  and  $|\downarrow\uparrow\downarrow\uparrow\rangle$  have been interchanged with those of  $|\downarrow\uparrow\uparrow\downarrow\rangle$  and  $|\uparrow\downarrow\downarrow\uparrow\rangle$ .

Similar observations apply also to the  $S = 0$  and  $S_z = 0$  remaining states that are orthogonal to  $\mathcal{X}_{00}^{(2)}$  [see  $\mathcal{X}_{00}^{(1)}$

in Eq. (28); case of double quantum dot] and to  $\mathcal{X}_{00}^{\text{RVB}}$  (case of a perfect square). The latter is given by<sup>13</sup>

$$\mathcal{X}_{00}^{\text{square,exci}} = -\frac{1}{2} |\uparrow\uparrow\downarrow\downarrow\rangle + \frac{1}{2} |\uparrow\downarrow\downarrow\uparrow\rangle + \frac{1}{2} |\downarrow\uparrow\uparrow\downarrow\rangle - \frac{1}{2} |\downarrow\downarrow\uparrow\uparrow\rangle. \quad (41)$$

In particular, one finds

$$\mathcal{X}_{00}^{(2)} = -\frac{1}{2} \mathcal{X}_{00}^{\text{RVB}} - \frac{\sqrt{3}}{2} \mathcal{X}_{00}^{\text{square,exci}} \quad (42)$$

and

$$\mathcal{X}_{00}^{(1)} = -\frac{\sqrt{3}}{2} \mathcal{X}_{00}^{\text{RVB}} + \frac{1}{2} \mathcal{X}_{00}^{\text{square,exci}}. \quad (43)$$

We note that the differences in the  $\mathcal{X}_{00}$  spin functions between the DQD case (corresponding to a parallelogram) and the perfect-square case are also reflected in the  $\mathcal{P}_{\uparrow\downarrow}$  CPDs. Indeed the CPDs of the DQD exhibit equal-height humps along the smaller side of the parallelogram while those of the perfect-square configuration (and/or circular quantum dot) exhibit equal-height humps along a diagonal.<sup>44</sup>

Néel antiferromagnetic ordering, where the average spin per site  $\langle S_j^z \rangle = (-1)^{j+1}/2$ , is an important magnetic phenomenon in the thermodynamic limit<sup>14</sup> associated with breaking of the total-spin symmetry. The finite size magnetic clusters discussed here exhibit a sharply different behavior in this respect. Indeed, as discussed in Ref. 14, the four-site Néel state is the single Slater determinant  $|\downarrow\uparrow\downarrow\uparrow\rangle$  (or  $|\uparrow\downarrow\uparrow\downarrow\rangle$ ). It is clear that the total-spin conserving EXD functions  $\mathcal{X}_{00}$  are multideterminantal and have an average spin per localized electron (per site)  $\langle S_j^z \rangle = 0$ .

We concur with Ref. 14 that the phenomenon of Néel antiferromagnetism is not applicable to assemblies of few electrons. In the next section, we argue that the appropriate concept for WM states is that of *spin entanglement*.

### B. Spin entanglement

In the previous sections, we showed that the EXD wave functions in the regime of Wigner-molecule formation can be approximated as a superposition of a small number of Slater determinants corresponding to well structured spin functions; see, e.g.,  $\mathcal{X}_{00}^{(1)}$  in Eq. (28). This is a great simplification compared to the initial EXD superposition [Eq. (7)], where the counting index is usually  $I \geq 500,000$ . This reduction of the molecular EXD solutions to their equivalent spin functions (described in Section VII) enables one to investigate their properties regarding fundamental quantum behavior associated with quantum correlations and fluctuations beyond the mean field.

The smallest number of Slater determinants contributing to the spin functions  $\mathcal{X}$ 's with  $S_z = 0$  is two. We

note that for  $S_z = 0$  a single determinant of four localized spin orbitals cannot conserve the total spin, and thus mean-field approaches like DFT (which are associated with a single determinant) are unable to describe quantum fluctuations and entanglement (see below). In particular, we note that the spin functions  $\mathcal{X}$ 's cannot be further reduced to simpler superpositions containing a smaller number of Slater determinants. As a result, they faithfully represent the extent of probabilistic quantum interconnection between the individual electrons participating in the system as described by an EXD solution. This quantum interconnection is widely referred to as *entanglement*<sup>46,47,48</sup> and generates correlations between the physical observables of the individual electrons (e.g., spins), even though the individual electrons are spatially separated. This existence of quantum interconnectivity independently of spatial separation has made entanglement the central instrument for the development of the fields of quantum information, such as quantum teleportation, quantum cryptography, and quantum computing. With their localized electrons, Wigner molecules in quantum dots offer another physical solid-state nanosystem where entanglement may be realized and studied.

The mathematical theory of entanglement is still developing and includes several directions. One way to study entanglement is through the use of properly defined measures of entanglement, e.g., the von Neumann entropy which utilizes the single-particle density matrix. Another way is to catalog and specify classes of entangled states that share common properties regarding multipartite entanglement. A well known class of  $N$ -qubit entangled states are the Dicke states,<sup>24,25,26,27</sup> which most often are taken to have the symmetric form:

$$\mathcal{X}_{N,k}^{\text{Dicke}} = \binom{N}{k}^{-1/2} (|\underbrace{11\dots 1}_k 00\dots 0\rangle + \text{Perm}). \quad (44)$$

Each qubit is a linear superposition of two single-particle states denoted by 0 or 1, and the symbol 'Perm' stands for all remaining permutations. The 0 or 1 do not have to be necessarily up or down 1/2-spin states. Two-level atoms in linear ultracold traps have already been used as an implementation of a qubit. Dicke states appear in many physical processes like superradiance and superfluorescence. They can also be realized with photons, where the qubits correspond to the polarization degree of freedom.<sup>27</sup>

In the 1/2-spin case of fermions (e.g., for electrons), the Dicke states of Eq. (44) correspond to a fully symmetric flip of  $k$  out of  $N$  localized spins. It is apparent that the four-qubit fully polarized ( $S = 2$  with spin projection  $S_z=0$ ) EXD solution is reproduced by  $\mathcal{X}_{20}$  of Eq. (17), and thus it is of the symmetric Dicke form (with  $k = 2$ ) displayed above in Eq. (44). On the other part, the DQD EXD states (with  $S_z = 0$ ) studied in Section VII with  $S = 0$  and/or  $S = 1$  represent a natural generalization of Eq. (44) to the class of *asymmetric* Dicke states. We hope that our results will motivate experimental research

aiming at the realization and control of such states in DQD electronic devices.

Before leaving this section, we note that Dicke states with a single flip ( $k = 1$ ) are known as  $W$  states.<sup>49,50</sup> For  $N = 4$  electrons, the latter states are related to EXD solutions with  $S_z = \pm 1$ . For the connection between  $W$  states and EXD states for  $N = 3$  electrons in anisotropic quantum dots, see Ref. 28.  $W$  states have already been realized experimentally using two-level ultracold ions in linear traps.<sup>51</sup>

## X. SUMMARY

Extensive investigations of lateral double quantum dots containing four electrons were performed using the exact-diagonalization method, as a function of interdot separation, applied magnetic field, and strength of inter-electron repulsion. Novel quantum behavior was discovered compared to circular QDs, concerning both energy spectra and quantum entanglement aspects. Thus it is hoped that the present work will motivate further experimental studies on lateral DQDs beyond the two-electron case.<sup>2,5</sup>

Specifically it was found that, as a function of the magnetic field, the energy spectra exhibit a low-energy band consisting of a group of six states, and that this number six is not accidental, but a consequence of the conservation of the total spin and of the ensuing spin degeneracies and supermultiplicities expressed in the branching diagram. These six states appear to cross at a single value of the magnetic field, and the crossing point gets sharper for larger interdot distances. As the strength of the Coulomb repulsion increases, the six states tend to become degenerate and a well defined energy gap separates them from the higher-in-energy excited states.

The formation of the low-energy band is a consequence of the localization of the four electrons within each dot (with two electrons on each dot). The result is formation (with increasing strength of the Coulomb repulsion) of a Wigner supermolecule, with the four localized electrons at the corners of a rectangular parallelogram. Using the spin-resolved pair-correlation functions, it was shown that one can map the EXD many-body wave functions to the spin functions associated with the four localized electrons. This mapping led us naturally to studying analogies with finite systems described by model Heisenberg Hamiltonians (referred to often as finite Heisenberg clusters). It was found that the determination of the equivalent spin functions enables investigations concerning the entanglement properties of the EXD solutions. In particular, it was shown that the formation of Wigner supermolecules generates strongly entangled states known in the literature of quantum information as  $N$ -qubit Dicke states.<sup>25,26,27</sup>

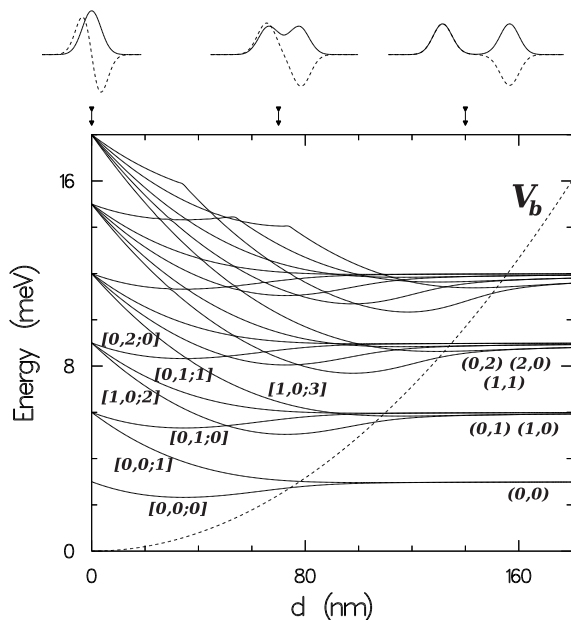


FIG. 12: Single-particle spectra of a double quantum dot at  $B = 0$  plotted versus the distance  $d$  between two (identical) coupled QDs with a TCO confinement  $\hbar\omega_{x1} = \hbar\omega_{x2} = \hbar\omega_y = 3$  meV and  $h_1 = h_2 = 0$  [see Eq. (1)]. For all  $d$ 's the barrier control parameters were taken as  $\epsilon_1^b = \epsilon_2^b = 0.5$ , i.e., the barrier height (depicted by the dashed line) varies as  $V_b(d) = V_0(d)/2$ . Molecular orbitals correlating the united ( $V_b = 0$ ) and separated-dots limits are denoted along with the corresponding (on the right) single-QD states. Wave function cuts at  $y = 0$  along the  $x$ -axis at several distances  $d$  (see arrows) corresponding to the lowest bonding and antibonding eigenvalues (solid and dashed lines, respectively) are displayed at the top. Energies in meV and distances in nm.

### Acknowledgments

This work was supported by the US D.O.E. (Grant No. FG05-86ER45234).

### APPENDIX: SINGLE-PARTICLE STATES OF THE TWO-CENTER OSCILLATOR

In this Appendix, we discuss briefly the energy spectra associated with the single-particle states of the two-center oscillator Hamiltonian given by Eq. (1). We follow here the notation presented first in Ref. 32. For further details, see Ref. 33.

The calculated two-center oscillator single-particle spectrum for a double quantum dot made of two tunnel-coupled identical QDs (with  $\hbar\omega_y = \hbar\omega_{x1} = \hbar\omega_{x2} = 3$  meV) plotted versus the distance,  $d$ , between the centers of the two dots, is given in Fig. 12. In these calculations, the height of the barrier between the dots varies as a function of  $d$ , thus simulating reduced tunnel coupling between them as they are separated; we take the barrier control parameter as  $\epsilon_1^b = \epsilon_2^b = 0.5$ . In the calculations

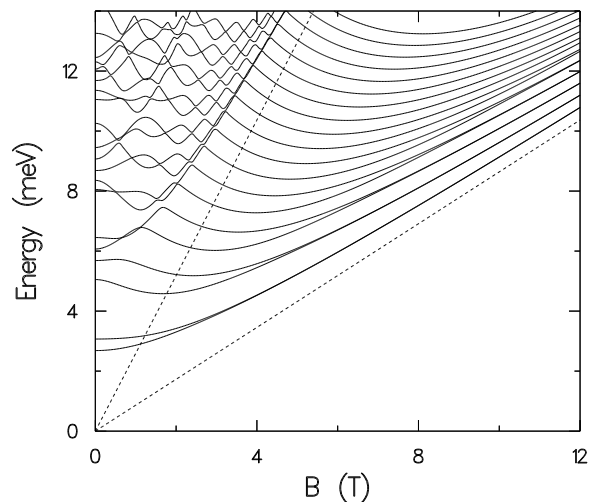


FIG. 13: Single-particle spectrum of the  $d = 70$  nm ( $\hbar\omega_{x1} = \hbar\omega_{x2} = \hbar\omega_y = 3$  meV,  $V_b = 2.43$  meV,  $h_1 = h_2 = 0$ ) double quantum dot versus  $B$  (in T). The  $\hbar\omega_c/2$  ( $\mathcal{N}_L = 0$ , lower line) and  $3\hbar\omega_c/2$  ( $\mathcal{N}_L = 1$ , upper line) first and second Landau levels are given by the dashed lines.

in this Appendix, we used GaAs values,  $m^* = 0.067m_e$  and a dielectric constant  $\kappa = 12.9$ . For the separated single QDs (large  $d$ ) and the unified QD ( $d = 0$ ) limits, the spectra are the same, corresponding to that of a 2D harmonic oscillator (being doubly degenerate for the separated single QDs) with a level degeneracy of 1, 2, 3, ... . In analogy with real molecules, the single-particle states in the intermediate region ( $d > 0$ ) may be interpreted as molecular orbitals (MOs) made of linear superpositions of the states of the two dots comprising the DQ. This qualitative description is intuitively appealing, though it is more appropriate for the weaker coupling regime (large  $d$ ); nevertheless we continue to use it for the whole range of tunnel-coupling strengths between the dots, including the strong coupling regime where reference to the states of the individual dots is only approximate. Thus, for example, as the two dots approach each other, the lowest levels ( $n_x, n_y$ ) with  $n_x = n_y = 0$  on the two dots may combine symmetrically (“bonding”) or antisymmetrically (“antibonding”) to form  $[0,0;0]$  and  $[0,0;1]$  MOs, with the third index denoting the total number of nodes of the MO along the interdot axis ( $x$ ), that is,  $2n_x + \mathcal{I}$ ,  $\mathcal{I} = 0$  or 1; for symmetric combinations ( $\mathcal{I} = 0$ ), this index is even and for antisymmetric ones ( $\mathcal{I} = 1$ ), it is odd. Between the separated-single-QDs and the unified-QD limits, the degeneracies of the individual dots’ states are lifted, and in correlating these two limits the number of  $x$ -nodes is conserved; for example the  $[0,0;1]$  MO converts in the unified-QD limit into the  $(1,0)$  state of a single QD, the  $[1,0;2]$  MO into the  $(2,0)$  state, and the  $[0,1;1]$  MO into the  $(1,1)$  state (see Fig. 12). Note that MOs of different symmetries may cross, while they do not if they are of the same symmetry.

In a magnetic field, the TCO model constitutes a gener-

alization of the Darwin-Fock model<sup>52</sup> for non-interacting electrons in a single circular QD. The single-particle spectra for the DQD ( $d = 70$  nm,  $V_b = 2.43$  meV) in a magnetic field ( $B$ ) are shown in Fig. 13 (here we neglect the Zeeman interaction which is small for our range of  $B$  values with  $g^* = -0.44$  for GaAs). The main features are: (i) the multiple crossings (and avoided crossings) as  $B$  increases, (ii) the decrease of the energy gap between levels, occurring in pairs (such as the lowest bonding-antibonding pair), portraying an effective reduced tun-

nel coupling between the QDs comprising the DQD as  $B$  increases, (iii) the “condensation” of the spectrum into the sequence of Landau levels  $(\mathcal{N}_L + 1/2)\hbar\omega_c$ ,  $\mathcal{N}_L = 0, 1, 2, \dots$  (the  $\mathcal{N}_L = 0$  and  $\mathcal{N}_L = 1$  bands are depicted, respectively, by the lower and upper dashed lines in Fig. 13). This is similar to the behavior of the single-particle Darwin-Fock spectrum for harmonically confined electrons in a circular QD<sup>52</sup> (note however that the geometry of the DQD is non-circular and deviates from a simple harmonic confinement).

- 
- \* Electronic address: Constantine.Yannouleas@physics.gatech.edu  
† Electronic address: Uzi.Landman@physics.gatech.edu
- 1 L.P. Kouwenhoven, D.G. Austing, and S. Tarucha, Rep. Prog. Phys. **64**, 701 (2001).
  - 2 R. Hanson, L.P. Kouwenhoven, J.R. Petta, S. Tarucha, and L.M.K. Vandersypen, Rev. Mod. Phys. **79**, 1217 (2007).
  - 3 P.A. Maksym, H. Imamura, G.P. Mallon, and H. Aoki, J. Phys.: Condens. Matter **12**, R299 (2000).
  - 4 S.M. Reimann and M. Manninen, Rev. Mod. Phys. **74**, 1283 (2002).
  - 5 C. Yannouleas and U. Landman, Rep. Prog. Phys. **70**, 2067 (2007).
  - 6 D. Loss and D.P. DiVincenzo, Phys. Rev. A **57**, 120 (1998).
  - 7 G. Burkard, D. Loss, and D.P. DiVincenzo, Phys. Rev. B **59**, 2070 (1999).
  - 8 R. Woodworth, A. Mizel, and D.A. Lidar, J. Phys.: Condens. Mat. **18**, S721 (2006).
  - 9 S. Tarucha, D.G. Austing, T. Honda, R.J. van der Hage, and L.P. Kouwenhoven, Phys. Rev. Lett. **77**, 3613 (1996).
  - 10 M. Ciorga, A.S. Sachrajda, P. Hawrylak, C. Gould, P. Zawadzki, S. Jullian, Y. Feng, and Z. Wasilewski, Phys. Rev. B **61**, R16315 (2000).
  - 11 M. Avinun-Kalish, M. Heiblum, O. Zarchin, D. Mahalu, and V. Umansky, Nature **436**, 529 (2005).
  - 12 P.V. Hendriksen, S. Linderth, and P.A. Lindgard, Phys. Rev. B **48**, 7259 (1993).
  - 13 S. Haas, in *Lectures on the Physics of Strongly Correlated Systems XII*, edited by A. Avella and F. Mancini (AIP Conf. Proceedings Vol. 1014, Melville, New York, 2008).
  - 14 P. Fazekas, *Lecture notes on electron correlation and magnetism* (World Scientific, Singapore, 1999).
  - 15 M.M. Tavernier, E. Anisimovas, F.M. Peeters, B. Szafran, J. Adamowski, and S. Bednarek, Phys. Rev. B **68**, 205305 (2003).
  - 16 M. Rontani, C. Cavazzoni, D. Bellucci, and G. Goldoni, J. Chem. Phys. **124**, 124102 (2006).
  - 17 A. Ghosal, A.D. Güclü, C.J. Umrigar, D. Ullmo, and H.U. Baranger, Phys. Rev. B **76**, 085341 (2007).
  - 18 M. Helle, A. Harju, and R.M. Nieminen, Phys. Rev. B **72**, 205329 (2005).
  - 19 L.X. Zhang, D.V. Melnikov, and J.P. Leburton, Phys. Rev. B **74**, 205306 (2006).
  - 20 B. Szafran, and F.M. Peeters, Phys. Rev. B **71**, 245314 (2005).
  - 21 T. Chwiej and B. Szafran, Phys. Rev. B **78**, 245306 (2008).
  - 22 R. Pauncz, *The Construction of Spin Eigenfunctions: An Exercise Book* (Kluwer Academic/Plenum Publishers, New York, 2000).
  - 23 C. Yannouleas and U. Landman, Phys. Rev. Lett. **82**, 5325 (1999); *ibid.* **85**, E2220 (2000).
  - 24 R.H. Dicke, Phys. Rev. **93**, 99 (1954).
  - 25 F. Verstraete, J. Dehaene, B. De Moor, and H. Verschelde, Phys. Rev. A **65**, 052112 (2002).
  - 26 J.K. Stockton, J.M. Geremia, A. C. Doherty, and H. Mabuchi, Phys. Rev. A **67**, 022112 (2003).
  - 27 J. K. Korbicz, O. Gühne, M. Lewenstein, H. Häffner, C. F. Roos, and R. Blatt, Phys. Rev. A **74**, 052319 (2006).
  - 28 Yuesong Li, C. Yannouleas, and U. Landman, Phys. Rev. B **76**, 245310 (2007).
  - 29 A three-dimensional magnetic-field-free version of the TCO has been used in the description of fission in metal clusters<sup>30</sup> and atomic nuclei.<sup>31</sup>
  - 30 C. Yannouleas and U. Landman, J. Phys. Chem. **99**, 14577 (1995). C. Yannouleas, R.N. Barnett, and U. Landman, Comments At. Mol. Phys. **31**, 445 (1995).
  - 31 J. Maruhn and W. Greiner, Z. Phys. **251**, 431 (1972). C.Y. Wong, Phys. Lett. **30B**, 61 (1969).
  - 32 R.N. Barnett, C.L. Cleveland, H. Häkkinen, W.D. Luedtke, C. Yannouleas, and U. Landman, Eur. Phys. J. D **9**, 95 (1999).
  - 33 The two-dimensional TCO was used earlier to approximate the solutions of the many-body Hamiltonian in Eq. (4) at the level of unrestricted Hartree-Fock (UHF) exhibiting breaking of total-spin symmetry, see Ref. 23; C. Yannouleas and U. Landman, Eur. Phys. J. D **16**, 373 (2001); Int. J. Quantum Chem. **90**, 699 (2002); J. Phys.: Condens. Matter **14**, L591 (2002). For a review of the necessary subsequent step of symmetry restoration, see Ref. 5.
  - 34 Due to the very long CPU times required for calculating surfaces, several CPDs at  $B = 0$  were calculated using  $K = 32$ . We checked that this does not influence our analysis of spin functions compared to  $K = 50$ .
  - 35 R.B. Lehoucq, D.C. Sorensen, and C. Yang, *ARPACK Users' Guide: Solution of Large-Scale Eigenvalue Problems with Implicitly Restarted Arnoldi Methods* (SIAM, Philadelphia, 1998).
  - 36 A. Szabo and N.S. Ostlund, *Modern Quantum Chemistry* (McGraw-Hill, New York, 1989).
  - 37 For the expression  $\mathcal{X}_{00}$  in Eq. (15), see Ch. 6.6 in Y. Suzuki and K. Varga, *Stochastic Variational Approach to Quantum-Mechanical Few-Body Problems* (Springer, Berlin, 1998). For the remaining two expressions for  $S_z = 0$ , i.e.,  $\mathcal{X}_{10}$  and  $\mathcal{X}_{20}$  [Eqs. (16) and (17), respectively; see Ying Li, Ph.D. Dissertation, Georgia Institute of Technology (2009)].
  - 38 C. Yannouleas and U. Landman, J. Phys.: Condens. Matter **14**, L591 (2002), in particular Fig. 3 therein.
  - 39 C. Yannouleas and U. Landman, Phys. Rev. B **69**, 113306 (2004).

- (2004).
- <sup>40</sup> C. Yannouleas and U. Landman, *Phys. Rev. Lett.* **85**, 1726 (2000).
- <sup>41</sup> V.A. Schweigert and F.M. Peeters, *Phys. Rev. B* **51**, 7700 (1995).
- <sup>42</sup> M.R. Geller and G. Vignale, *Phys. Rev. B* **53**, 6979 (1996).
- <sup>43</sup> E. Manousakis, *Rev. Mod. Phys.* **63**, 1 (1991).
- <sup>44</sup> C. Shi, G.S. Jeon, and J.K. Jain, *Phys. Rev. B* **75**, 165302 (2007).
- <sup>45</sup> Ph. Anderson, *Physics Today* (April 2008) p. 8
- <sup>46</sup> E. Schrödinger, *Proc. Cambridge Phil. Soc.* **31**, 555 (1935).
- <sup>47</sup> A. Einstein, B. Podolsky, and N. Rosen, *Phys. Rev.* **47**, 0777 (1935).
- <sup>48</sup> L. Amico, R. Fazio, A. Osterloh, and V. Vedral, *Rev. Mod. Phys.* **80**, 517 (2008).
- <sup>49</sup> W. Dür, G. Vidal, and J.I. Cirac, *Phys. Rev. A* **62**, 062314 (2000).
- <sup>50</sup> V. Coffman, J. Kundu, and W.K. Wootters, *Phys. Rev. A* **61**, 052306 (2000).
- <sup>51</sup> H. Häffner, W. Hänsel, C.F. Roos, J. Benhelm, D. Chekalkar, M. Chwalla, T. Körber, U.D. Rapol, M. Riebe, P.O. Schmidt, C. Becher, O. Gühne, W. Dür, and R. Blatt, *Nature* **438**, 643 (2005).
- <sup>52</sup> V. Fock, *Z. Phys.* **47**, 446 (1928); C.G. Darwin, *Proc. Cambridge Philos. Soc.* **27**, 86 (1930).